Physics in Medicine & Biology

PAPER • OPEN ACCESS

Experimental exploration of a mixed helium/carbon beam for online treatment monitoring in carbon ion beam therapy

To cite this article: L Volz *et al* 2020 *Phys. Med. Biol.* **65** 055002

IOP Publishing Phys. Med. Biol. 65 (2020) 055002 (14pp) https://doi.org/10.1088/1361-6560/ab6e52

Physics in Medicine & Biology

IPEM Institute of Physics and Engineering in Medicine

RECEIVED
17 October 2019

REVISED
22 December 2019

ACCEPTED FOR PUBLICATION
21 January 2020

PUBLISHED
28 February 2020

PAPER

Experimental exploration of a mixed helium/carbon beam for online treatment monitoring in carbon ion beam therapy

L Volz[1,2,8], L Kelleter[3,8], S Brons[5], L Burigo[6,7], C Graeff[4], N I Niebuhr[2,6,7], R Radogna[3], S Scheloske[5], C Schömers[5], S Jolly[3] and J Seco[1,2]

[1] Department of Biomedical Physics in Radiation Oncology, German Cancer Research Centre (DKFZ), Heidelberg, Germany
[2] Department of Physics and Astronomy, Heidelberg University, Heidelberg, Germany
[3] Department of Physics and Astronomy, University College London, London, United Kingdom
[4] Biophysics Division, GSI Helmholtzzentrum für Schwerionenforschung GmbH, Darmstadt, Germany
[5] Heidelberg Ion-Beam Therapy Centre (HIT), Heidelberg, Germany
[6] Department of Medical Physics in Radiation Oncology, German Cancer Research Centre (DKFZ), Heidelberg, Germany
[7] Heidelberg Institute for Radiation Oncology (HIRO), National Centre for Radiation Research in Oncology (NCRO), Heidelberg, Germany
[8] Authors contributed equally.

E-mail: l.volz@dkfz-heidelberg.de and laurent.kelleter@ucl.ac.uk

Keywords: 4D treatment monitoring, carbon therapy, range verification, helium imaging, mixed beam

Abstract

Recently, it has been proposed that a mixed helium/carbon beam could be used for online monitoring in carbon ion beam therapy. Fully stripped, the two ion species exhibit approximately the same mass/charge ratio and hence could potentially be accelerated simultaneously in a synchrotron to the same energy per nucleon. At the same energy per nucleon, helium ions have about three times the range of carbon ions, which could allow for simultaneous use of the carbon ion beam for treatment and the helium ion beam for imaging. In this work, measurements and simulations of PMMA phantoms as well as anthropomorphic phantoms irradiated sequentially with a helium ion and a carbon ion beam at equal energy per nucleon are presented. The range of the primary helium ion beam and the fragment tail of the carbon ion beam exiting the phantoms were detected using a novel range telescope made of thin plastic scintillator sheets read out by a flat-panel CMOS sensor. A 10:1 carbon to helium mixing ratio is used, generating a helium signal well above the carbon fragment background while adding little to the dose delivered to the patient. The range modulation of a narrow air gap of 1 mm thickness in the PMMA phantom that affects less than a quarter of the particles in a pencil beam were detected, demonstrating the achievable relative sensitivity of the presented method. Using two anthropomorphic pelvis phantoms it is shown that small rotations of the phantom as well as simulated bowel gas movements cause detectable changes in the helium/carbon beam exiting the phantom. The future prospects and limitations of the helium/carbon mixing as well as its technical feasibility are discussed.

1. Introduction

The advantage of carbon-beam therapy over conventional photon radiotherapy lies in the ion's highly localised depth-dose deposition, with a low entrance dose increasing to a maximum—the Bragg peak—beyond which there is a sharp reduction in dose deposition. However, the steep dose gradient at the end of the particle range in matter makes ion beam therapy sensitive to range uncertainties arising, for example, from inter- and intra-fractional anatomical changes, uncertainties at the treatment planning stage as well as the patient setup. In current clinical practice, range uncertainties are accounted for by adding safety margins around the tumour volume (Paganetti 2012) and by avoiding beam directions corresponding to the ions stopping directly in front of an organ at risk (OAR). However, even with safety margins, intra-fractional motion can lead to severe target dose deterioration and/or over-dosage of healthy tissue (Bert *et al* 2008, Seco *et al* 2009, Dolde *et al* 2018).

In order to exploit the full potential of ion beam radiotherapy, therefore, improved methods for inter- and intra-fractional treatment verification are needed. Several methods for treatment verification have been proposed of which prompt gamma imaging (Hueso-González *et al* 2018) and in-beam PET imaging (Ferrero *et al* 2018) are promising candidates. A detailed overview can be found in Parodi and Polf (2018).

Recently, it has been proposed that a small percentage of helium ions could be added to a carbon ion treatment beam for online treatment monitoring (Graeff *et al* 2018, Mazzucconi *et al* 2018). The approximately equal mass/charge ratio of fully stripped helium and carbon ions (relative difference $\approx$0.065%), could enable their simultaneous acceleration in a synchrotron accelerator to the same velocity (same energy per nucleon). Due to the helium ions' $\sim$3 times larger range compared to that of carbon ions at the same velocity, treatment with a carbon ion beam and simultaneous treatment monitoring with helium ions could be possible. In fact, the similarity in accelerator settings for the delivery of a mixed helium/carbon beam ($^{12}C^{4+}$ with $^{3}He^{+}$) has been reported already in Kanai *et al* (1997) for a cyclotron facility for the purpose of treatment with beams of mixed relative biological effectiveness (RBE) but without consideration for online treatment monitoring. Recently, Graeff *et al* (2018) have shown the potential of using a mixed helium/carbon beam as a range probe for carbon ion treatment investigating lung patient cases based on 4D treatment planning. Assuming a fixed helium contamination in the primary carbon ion beam during the plan optimisation, they showed that the additional RBE dose stemming from a 10% helium contamination in the primary beam would make up less than 0.5% of the target RBE dose. This stems from the physical dose difference between the plateau region of the helium ion depth dose profile and the carbon Bragg peak, as well as the difference in RBE. Moreover, the dose deposited in the patient distal to the tumor stemming from the additional helium contamination was also smaller compared to that deposited by the carbon fragments. The idea of a mixed beam for treatment monitoring was first explored experimentally in the study presented recently by Mazzucconi *et al* (2018). In their proof-of-concept work, they demonstrated that for a 10% mix of helium ions in the carbon beam, the helium residual range could be detected in a scintillation detector despite the signal contamination with carbon fragments. However, all experimental tests presented were conducted using protons in place of helium ions and no anthropomorphic cases were investigated.

The aim of this work was therefore to experimentally corroborate the results by Graeff *et al* (2018) and Mazzucconi *et al* (2018) using sequentially irradiated beams of helium and carbon ions at the Heidelberg Ion-Beam Therapy Centre (HIT). The beam was monitored using a novel range telescope developed at University College London (UCL). First, the system's sensitivity was assessed with simple PMMA degraders with differently sized air gaps. For assessing more clinically relevant scenarios, prostate cancer treatments were investigated. With the ADAM pelvis phantom (Niebuhr *et al* 2019), the feasibility of using a mixed helium/carbon beam to detect rectal gassing/bowel gas movements was investigated. The recently developed ADAM-PETer pelvis phantom (Homolka *et al* 2019) was used to simulate small patient rotations. The acquired data allow to draw conclusions on the clinical application and the limitations of the helium/carbon beam mixing method.

2. Materials and methods

2.1. Range telescope

The range of the primary helium ions and the fragments produced by the carbon ion beam were monitored using a novel range telescope developed at UCL for proton range quality assurance. This detector will be detailed in a separate publication currently under preparation. The prototype detector consisted of a stack of 49 polystyrene-based plastic scintillator sheets of 2–3 mm thickness, covered an area of $10 \times 10\,\text{cm}^2$, and had a relative stopping power (RSP) of 1.025. The detector covered a total water equivalent thickness (WET) range of $\sim$127 mm. Each sheet was painted black in order to avoid light contamination into neighbouring sheets. The resulting thickness of paint was taken into account in the calculation of the absolute WET.

A large-area CMOS sensor with an active area of $150 \times 100\,\text{mm}^2$ and a pixel size of 100 μm was used for the readout of the scintillation light. The detector readout frame rate was 25 Hz (40 ms exposure time). The detector was placed in a light-tight enclosure with two beam entrance/exit windows made of aluminum coated Mylar polyester foil on both ends of the scintillator stack.

Before the measurements, the detector was calibrated by shooting high-energy beams of carbon ions (E = 430 MeV/u) as well as helium ions (E = 220 MeV/u) through the scintillator stack from both sides of the detector. In data processing, these shoot-through measurements were then used to correct for non-uniformity in the light output of each individual detector sheet for each ion species. Additionally, a background measurement was acquired to determine the signal in the absence of scintillation light.

It is important to note that the range telescope measures scintillation light and not dose. The plastic scintillator used in the range telescope exhibits quenching effects that can be described by Birks' law (Birks 1951). The measured depth-light curves presented in this work were not corrected for quenching: however, the simulated energy deposits were converted to depth-light curves using Birks' law (see section 2.4). Additionally, the measured light output of the detector depends on the lateral position at which the beam enters the detector. In this work, the detector position relative to the beam was not changed between measurements.

2.2. Investigated phantoms

Three different phantom setups were investigated in this study. The sensitivity and limitation of the method was assessed quantitatively using simple PMMA phantoms. For qualitatively investigating the use of a mixed helium/carbon beam in clinically relevant scenarios, different motion scenarios were explored using two anthropomorphic phantoms. Treatment planning x-ray CT scans of the anthropomorphic phantoms were acquired at the Siemens Somatom Definition Flash scanner of the German Cancer Research Centre (DKFZ, Heidelberg).

2.2.1. PMMA phantom

First, several PMMA slabs were arranged upstream of the range telescope to quantify the sensitivity of the method in a controlled setting. Accurate WET values for each of the slabs were available from PTW Peakfinder measurements (Arico 2016). In order to create a range shift in the beam, two thin PMMA slabs of similar WET were placed at a depth of 49.6 mm PMMA (57.64 mm WET) such that they formed a vertical slit of adjustable opening width (2–5 mm). Different PMMA slabs were used to create variable gap thicknesses (1–5 mm). The total WET of the setup (without gap) was 219.59 mm for all measurements. The schematic setup is shown in figure 1.

2.2.2. ADAM phantom

The ADAM (anthropomorphic deformable and multi-modal) Pelvis Phantom (Niebuhr *et al* 2019) was used to demonstrate the effect of rectal gassing/bowel gas movements on the helium range. The phantom consists of various tissue equivalent materials enclosed in an elliptical PMMA container (370 mm major, 220 mm minor axis) and closely models the anatomical structure of a male pelvis. The phantom features a fully deformable and movable prostate, an inflatable rectum and a deformable bladder, as well as the pelvic bone structures. To simulate rectal gassing/bowel gas movements, a rectal balloon was inserted into the phantom's rectum such that the balloon was located next to the prostate. The balloon was inflated to air volumes of 30 ml, 45 ml and 60 ml. The uncertainty on the air volume was estimated to be $\sim$5 ml from the retained air volume after irradiation. Liquid fillings were not yet possible with the phantom and the rectum was not collapsed when the rectal balloon was not inflated, but retained a residual volume.

2.2.3. ADAM-PETer phantom

In order to investigate the effect of patient rotations, the recently developed second generation of the ADAM phantom, named ADAM-PETer (Homolka *et al* 2019), was used. Compared to the ADAM phantom, the ADAM-PETer phantom has a smaller container (310 mm major, 195 mm minor axis), denser and more realistic bone structures as well as a 3D printed prostate. The reason for using both available ADAM phantoms in this study resides in their respective advantages/disadvantages. The ADAM phantom hull was made from two separate PMMA pieces that are glued together on both lateral sides (see figure 2). Additionally, the thickness gradient of the ADAM phantom hull is larger compared to that of the newer ADAM-PETer phantom. Hence, for investigation of patient rotations/motion, observed effects could stem from the glue or the phantom shape, rather than anatomical features which would not resemble a realistic scenario. However, the available version of the ADAM-PETer phantom did not feature a fully deformable/movable prostate and rectum, which would have been unfavourable for the investigation of rectal gassing.

2.2.4. Treatment planning

For the anthropomorphic pelvis phantoms, treatment plans were generated using the MatRad open source treatment planning platform (Wieser *et al* 2017). A dose of 2 Gy RBE per fraction was planned for the target (whole prostate). The spot spacing was set to 3 mm. No OARs were considered and no margins were set around the target volume. The additional dose from the helium beam was not considered in the treatment optimization. The minimum and maximum beam energy in the plan as well as planned beam angles are listed in table 1. The prostate was positioned in the beam isocentre in all cases.

2.3. Beam settings

Experiments were conducted at the HIT experimental room (Haberer *et al* 2004). Since a real mixed beam could not yet be delivered, the experiments were conducted with sequentially irradiated helium and carbon ion beams of similar energy/nucleon and similar spot size. The measurements from the sequentially irradiated beams were mixed offline which will be detailed in section 2.5. The generation of a mixed beam will be discussed in

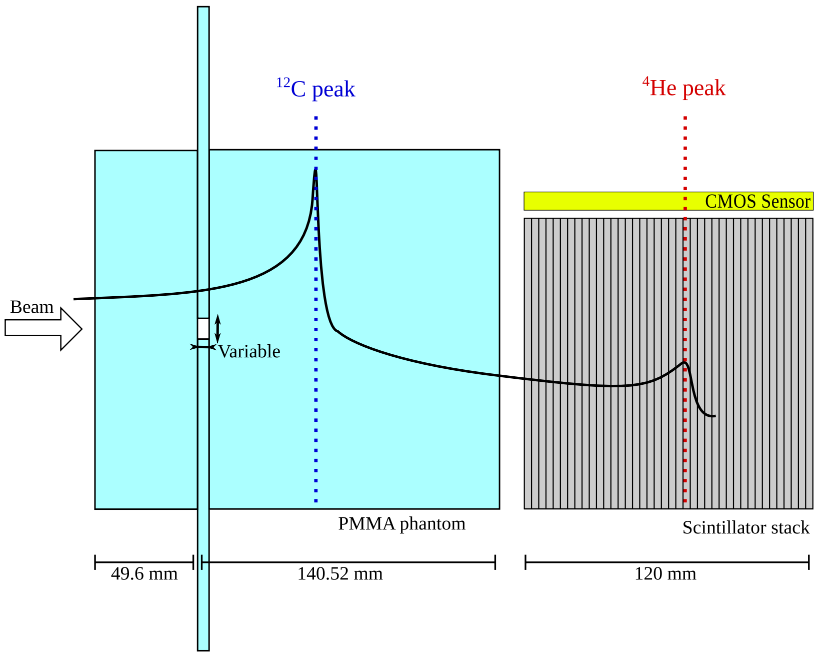

Figure 1. Schematic depiction of the PMMA setup used to investigate the sensitivity of the helium/carbon beam mixing method (not to scale). The total thickness of the PMMA setup was 190.12 mm (219.59 mm WET), the PMMA blocks had a width and height of 150 mm. Two PMMA slabs of equal thickness were used to create a vertical slit of variable width/thickness at a depth of 49.6 mm in the setup. For the investigated energy in this work, the carbon peak was located at a water equivalent depth of ∼99 mm, with the helium peak was located at 305 mm water equivalent depth.

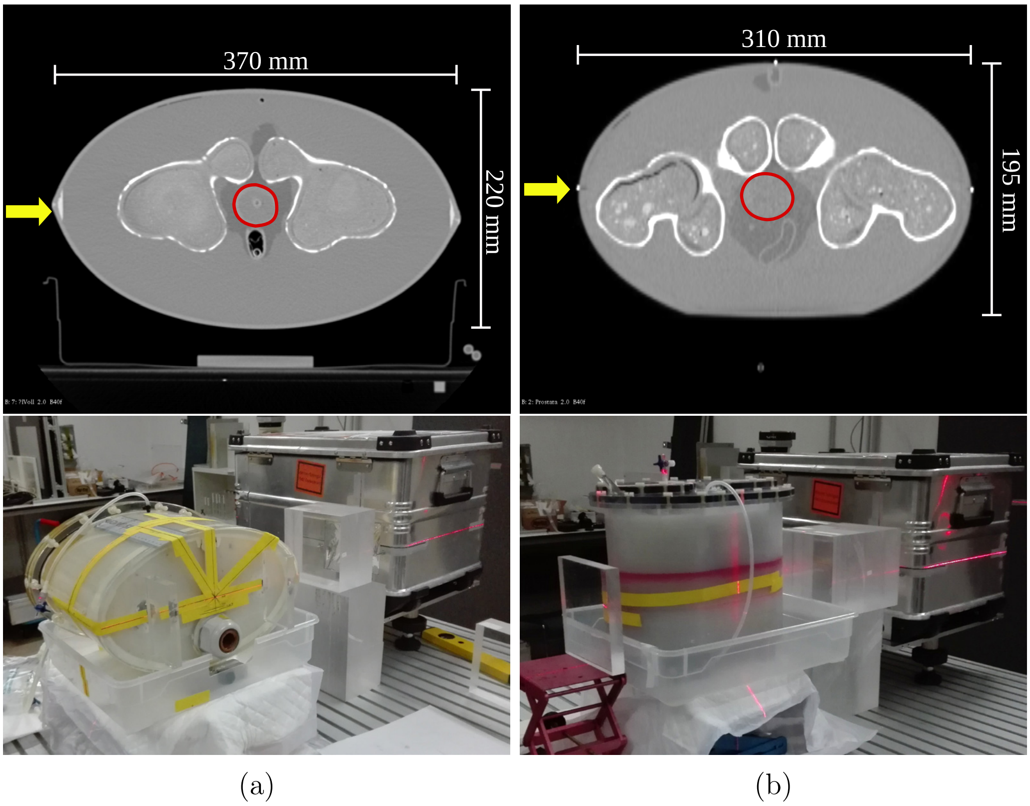

Figure 2. Isocentrical axial slice through CT images of the used phantoms (top), and photographs of the experimental setup (bottom): (a) ADAM phantom and (b) ADAM-PETer phantom. The area outlined in red on the CT scans marks the target (prostate), the yellow arrow indicates the beam direction.

Table 1. Treatment plan minimum and maximum energies for the different phantoms. The 0° gantry angle refers to a vertical beam direction.

Phantom	Gantry angle (°)	Min. E (MeV/u)	Max. E (MeV/u)
ADAM	[90, −90]	300	355
ADAM-PETer	[90, −90]	260	316

Table 2. Beam settings for the different experimental setups investigated in this work. The beam focus is given as the beam FWHM at the isocentre.

	Energy (MeV/u)		Focus (mm)		Intensity (part. s^{-1})	
Setup	^{12}C	^{4}He	^{12}C	^{4}He	^{12}C	^{4}He
PMMA phantom	219.8	220.5	8.5	8.1	8×10^7	8×10^7
ADAM/ADAM-PETer	324.26	324.26	8.0	7.0	8×10^7	7×10^8

section 4.3. For all measurements, a 3 mm ripple filter was used following the common practice with carbon ion treatments at HIT. The detailed beam settings for the respective phantom setups are listed in table 2.

Energies up to ∼220 MeV/u were available for both carbon and helium ions from the standard libraries of beam characteristics used at HIT (Kleffner *et al* 2009). As no perfect match between helium and carbon ion beam settings existed in these tables, the closest representation was chosen for the PMMA measurements. The highest clinically available beam intensity of 8×10^7 particles s^{-1} for carbon ions would—assuming a constant ratio of 10:1 between primary carbon and helium ions—correspond to an intensity of 8×10^6 particles s^{-1} for helium ions in the mixed beam. This is lower than the lowest helium intensity available from the standard settings. Since the runs were mixed off-line in data processing, the same intensity was therefore chosen for both ion types. The impact of this is discussed in section 4.

Due to the high carbon beam energy required for the treatment of the prostate targets within the pelvis phantoms, a helium beam with manual settings had to be used, since the corresponding high helium energies are not available from the standard beam libraries at HIT which cover a maximum range in water of 30 cm for the different ion species. However, since the HIT synchrotron was designed for the acceleration of carbon ions up to 430 MeV/u, the synchrotron has the potential to accelerate helium ions (and protons) to higher energies than those used clinically. Helium ion beams, with higher energies than needed for therapy, have recently been established at HIT in a preliminary version, for a few energies only and without scanning capability or position and intensity control. In this work, a helium beam at 324. 26 MeV/u was used, with an intensity of 7×10^8 particles s^{-1} and a beam focus of 7 mm FWHM.

For the ADAM-PETer phantom, a 20 mm PMMA slab was added before the setup, as the available high helium energy would have been above the energies set by the treatment plan. With the PMMA slab, the mean beam energy was reduced to ∼297 MeV/u for carbon ions (value obtained from the simulation described below), corresponding to the high energy part of the respective treatment plan.

2.4. Monte Carlo simulation

In order to validate the acquired measurements and to further exploit the potential of the helium/carbon beam mixing technique, Monte Carlo simulations using Geant4 version 10.05.0 (Agostinelli *et al* 2003, Allison *et al* 2006, 2016) were conducted. In detail, the following physics lists were activated: G4DecayPhysics, G4StoppingPhysics for nuclear capture at rest, G4EmExtraPhysics and G4EmStandardPhysics_option4 for accurate modelling of low energy electromagnetic interactions, G4HadronElasticPhysics for modelling of elastic nuclear interactions. To model inelastic nuclear interactions the G4QMDReaction model was chosen for carbon ions as recommended by Böhlen *et al* (2010) and Dudouet *et al* (2014). For helium ions, G4BinaryLightIonReaction was activated together with the Tripathi cross section data (Tripathi *et al* 1999) recently tuned by Horst *et al* (2019) to accurately model the helium Bragg peak. The default production cuts (affecting electrons and photons) were set in the simulation to 1 mm. Within the range telescope a finer step limit and finer production cuts (both 0.05 mm) were set.

The helium and carbon energy spectra after the 3 mm ripple filter were modelled from the generic beam line presented in Wieser *et al* (2017). The beam monitoring chambers were modelled in the generic beam line using a water slab of 2.03 mm thickness. The distance between nozzle and isocentre was 1.02 m (air, RSP =0.001). Therefore, the WET the beam crossed before reaching the isocentre was 3.05 mm. The lateral beam profile was modelled with a 2D Gaussian spatial distribution with the FWHM set in the experiments. The initial beam divergence was neglected in the simulation.

The detector was modelled as a single $100 \times 100 \times 120$ mm^3 block of polystyrene using the polystyrene material composition from the NIST database (Berger *et al* 2005) and modifying the density to match the known

Table 3. Chemical composition of the different materials used the anthropomorphic phantoms as implemented in the simulation. The HUs mark the lower-bound thresholds used for assigning a given material to voxel in the CT scans. The corresponding modelled patient tissue is given for each material.

Material	HU	Element (weight (%))	Tissue
Peanut oil	−160	H(7.36);C(58.94);N(20.62);O(13.08)	Adipose
Agarose1	−30	H(10.57);C(0.94);O(84.49);Na(2.19);F(1.81)	Muscle
Agarose3	35	H(10.82);C(1.65);O(86.53);Na(0.55);F(0.45)	Prostate
Vaseline/K_2HPO_4	80	H(5.52);C(64.6);N(5.02);O(9.19);P(4.45);K(11.22)	Inner bone
Gypsum	285	O(47.01);Ca(29.44);S(23.55)	Cortical bone

RSP of 1.025. Within the simulation, the energy deposit in the detector was binned along the condensed-history steps into a histogram for which the bins corresponded to the sheets of the prototype[9]. In order to accurately model the light output of the experimental measurement, the scintillation light quenching has been approximated using Birks' law (Birks 1951). The scintillation light output S is given as:

$$S \propto \int \frac{\mathrm{d}E/\mathrm{d}x}{1 + kB\mathrm{d}E/\mathrm{d}x}\mathrm{d}x \tag{1}$$

where Birks' constant was determined as $kB = 0.075 \pm 0.01$ mm MeV^{-1} by comparing proton beam measurements with the detector and HIT base data proton depth dose curves (unpublished data). To accurately model the detector response across the transverse plane, S would need to be scaled by the scintillation light yield of the detector and an additional correction factor accounting for spatial variations in the detector response. The additional scaling factors that describe the light output of the detector are omitted here, as the signals were normalised in data processing.

The PMMA degrader slabs were simulated using the NIST PMMA material composition, setting the density such that the WET of the simulated slabs matched the WET of the experimental slabs. For the anthropomorphic phantoms, voxelised digital geometries were created from the treatment planning x-ray-CT scans. The phantom materials were implemented from their chemical composition using the material description in Niebuhr *et al* (2019) and Niebuhr *et al* (2016). See table 3 for a detailed list. First, for each Hounsfield unit (HU) in the CT scan, a material was assigned based on the thresholds listed in table 3. Then the relative electron density corresponding to the HU was calculated from the HU lookup table of the CT scanner used to produce the treatment planning CTs. The relative electron density was converted to physical density following equation (1) in Collins-Fekete *et al* (2017). This was then used to assign a material and density to each voxel of the CT scan. For all voxels with a HU below −160 the assigned material was air at density 1.155 mg cm^{-3}.

For the anthropomorphic phantoms, additionally the dose deposit in each voxel was recorded in the simulation. The dose in lateral direction was then summed up to display the integral dose to the patient as function of the distance to the isocentre.

All simulation results shown in this work were generated using 10^6 primary carbon ions and 10^5 primary helium ions.

2.5. Data processing and offline beam mixing

In the experiment, helium and carbon beams were irradiated consecutively. The experimental results shown in this work always represent a 'snapshot' of the beam: i.e. the sum of twenty-one image frames corresponding to a total acquisition time of 0.84 s. Depth-light curves were generated from the background-corrected images by summing up the light yield in a scintillator sheet and attributing it to the WET at the centre of the sheet. The light yield is calibrated with two shoot-through curves of the same ion taken from both sides of the range telescope in order to correct for the differences in the signal of the scintillator sheets. The depth-light curves of the helium and carbon beams were scaled according to a 10:1 carbon:helium ratio and summed up in order to produce the signal of a mixed beam. In the simulation, the recorded signals were simply summed as a factor 10 smaller number helium primaries compared to carbon had already been generated. Figure 3 shows the resulting depth-light curves of helium, carbon and the mixed helium/carbon beam. The curves were normalized to the combined helium/carbon signal in the first scintillator sheet. Small differences are due to the fluctuations in the measured carbon signal in the first couple of scintillator sheets.

[9] The prototype features 2 mm, 2.6 mm as well as 3 mm sheets. In the simulation, a constant binning of 3 mm was used.

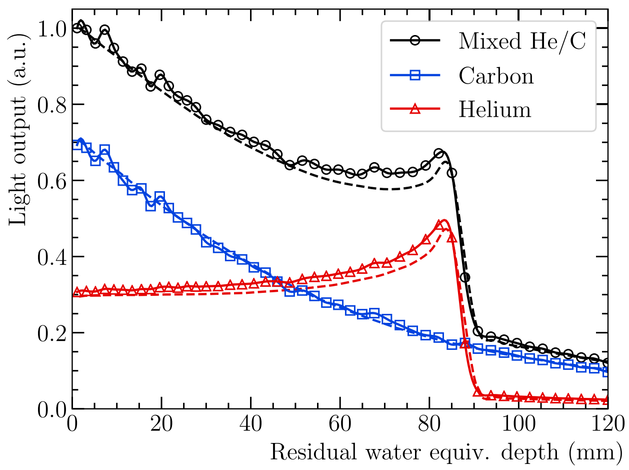

Figure 3. Example of helium (red) and carbon (blue) depth-light curves used for off-line helium/carbon beam mixing (black) at 220 MeV/u and the PMMA setup without gap: measurement (solid) and simulation (dashed). The measured signal for helium was scaled down to match a 10:1 ratio to the carbon primaries.

3. Results

In this section, the results from the irradiation of the phantoms introduced in section 2.2 are presented. Both measurement and simulation results are presented side by side for comparison. The relative difference between the curve of interest $f(x)$ and a reference curve $g_{\mathrm{ref}}(x)$ was chosen as a metric to quantify the change in the measured signal. It is defined as $[f(x) - g_{\mathrm{ref}}(x)]/g_{\mathrm{ref}}(x)$. This enables displaying very small differences between the curve of interest and the reference curve, emphasising the sensitivity of the helium/carbon beam mixing. In all plots, the horizontal axis represents the residual water equivalent range of the beam measured in the scintillator stack. The depth-light curves were normalised to the signal in the first scintillator sheet of the reference measurement in order to enable easier comparison between experiment and simulation.

3.1. PMMA phantom

In figure 4, the effect of air slits of variable width and thickness are shown. At 2 mm gap thickness, the 5 mm and 2 mm slit widths resulted in respective relative differences of 40% and 17%. This is expected since, with increasing slit width, a larger fraction of beam particles crosses the slit. For the 8 mm FWHM beam, approximately 55% of the beam particles cross the slit opened to 5 mm width, while only $\sim$22% of particles traverse the slit in the case of an opening width of 2 mm. It can be seen in figure 4 (bottom) that the observed peak width in the relative difference is proportional to the slit thickness. However, this relation is perturbed by the finite slope of the helium peak and the limited spatial resolution of the range telescope. In all cases, the mixed depth-light curve changed only slightly with the introduction of the air gaps and those changes were only observable in the high-gradient region at the helium peak. In the case of a 1 mm thick, 2 mm wide slit the resulting maximum relative difference was 8%.

3.2. ADAM phantom

The ADAM phantom was irradiated at three different spots in the same iso-energy layer: the tumour isocentre, a spot close to the rectum according to the treatment planning system (vertical position: isocentre−18 mm; horizontal position: isocentre + 6 mm) and a spot in between the two (vertical position: isocentre−12 mm; horizontal position: isocentre). The spot positions and the different rectal fillings are shown in figure 5.

Figure 6 shows the artificially mixed helium/carbon signals. For the spot close to the rectum, a change in the helium range was observable even for the smallest air volume filled in the rectal balloon. Since the rectum did not collapse when the rectal balloon was not inflated, the lowest filling of the rectal balloon resulted only in a small change of the diameter of the rectum compared to the reference state. For larger fillings of the rectum, a drastic overshoot was observed in the helium range as the beam crossed into the rectum and the rectal gas. Similarly, for the spot located between isocentre and the rectal wall, the two larger rectal balloon fillings resulted in observable changes in the helium signal. For the spot in the isocentre, no significant change was observed for either air filling in the measurement. In the simulation, however, small changes were observed for the two larger air fillings. This disagreement could likely be attributed to changes in the relative distance of the spot centre to the urethra stemming from position uncertainties and/or motion of the prostate between the treatment planning CT and the irradiation. In the phantom the urethra is modelled with a silicone pipe. As such, the rectal balloon filling pushing the pipe wall out of the beam might have caused the observed range change in the simulation (compare

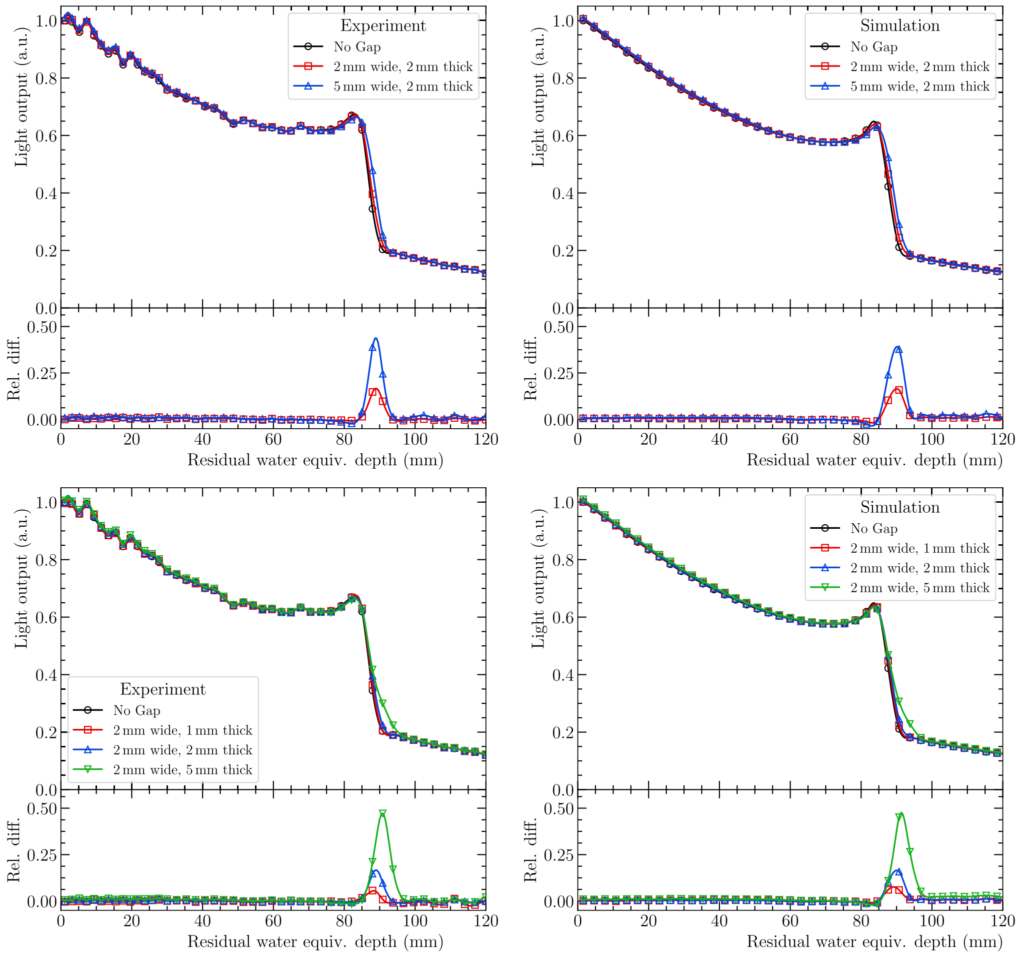

Figure 4. Result of introducing an air-filled slit of width 2–5 mm and thicknesses of 2 mm and 5 mm (top), as well as a fixed width of 2 mm and thickness of 1 mm–5 mm (bottom) in the beam path: measurement (left) and simulation (right).

figure 5). The measurements of the other two spots qualitatively agree well with the simulation. Additionally, the simulation shows that the position of the helium peak in the detector correlates well with the changes in carbon dose in the patient (compare figures 6(b) and (c)). This correlation is essential for drawing conclusions on the carbon dose from the mixed helium/carbon beam signal in the detector.

3.3. ADAM-PETer phantom

In order to demonstrate the effect that a small patient rotation would have on the observed helium/carbon mixed signal, the ADAM-PETer phantom was used in its upright position, with the phantom rotated manually by 2° and 4° around the vertical axis. The results can be seen in figure 7. Both rotations lead to a noticeable change in the measured mixed beam signal. A similar, yet slightly larger effect can be observed in the simulation. In the depth-dose profile shown in figure 7(c), in addition to the range shift in the carbon peak, differences starting at the position corresponding to the entrance of the hip bone (at ∼135 mm upstream from the isocentre) can be seen. As such, it can be argued that the observed shift in the carbon range stems from the rotation of the hip bone.

4. Discussion

4.1. Uncertainty sources

4.1.1. Detector readout and data processing

Due to the high resolution of the CMOS sensor and the high light output of the scintillator, the statistical uncertainty on the light yield in a single sheet is low, <1% for carbon and helium.

However, the particle-specific calibration of the detector introduced a systematic uncertainty, which was the same for all recorded curves of the same particle. This uncertainty is estimated to be <3% by comparing the shoot-through curves for protons, helium and carbon ions.

Furthermore, the carbon depth-light curves were acquired at a very low beam intensity compared to the calibration shoot-through curves. This intensity mismatch is likely to be responsible for the fluctuations seen in the

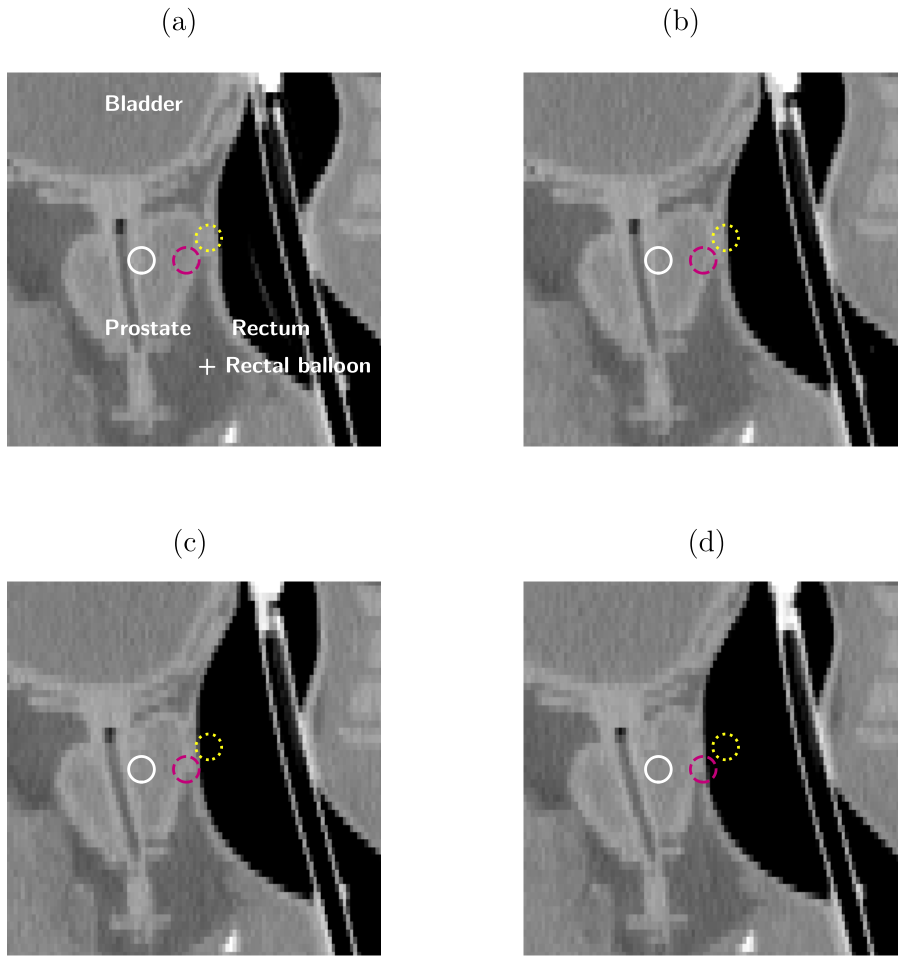

Figure 5. Sagittal plane of the ADAM phantom CT scans for different stages of inflation of the rectal balloon. The circles indicate the 2σ region of the irradiated carbon ion beam spots at the isocentre (white solid), close to the rectum (yellow dotted) and in between (magenta dashed). (a) No inflation. (b) 30 ml inflation. (c) 45 ml inflation. (d) 60 ml inflation.

carbon signal (and therefore also in the mixed signal, see figure 3) close to the entrance of the scintillator stack. These fluctuations are consistently the same for all measured depth-light curves (see figures 4, 6 and 7). The magnitude of the systematic uncertainty in the low-intensity carbon signal is on the order of 5%.

4.1.2. *Particle rate*

The mixing of the sequentially irradiated helium and carbon beam in data processing required a stable particle rate to match a 10:1 ratio between the carbon and helium signal. While this was the case for the standard beam settings used, for the experimental beam parameters, fluctuations up to 15% were observed between spills. For the experimental helium settings, no spill regulation was active, likely causing these fluctuations. Hence, before adding the helium and carbon signals together, for the pelvis phantom measurements, the helium signals were scaled such that the signal in the first couple of sheets matched the reference measurement for each phantom. As this normalisation step can only cause an underestimation of signal changes, it does not affect the conclusion on the usefulness of the helium/carbon beam mixing method.

4.1.3. *Beam parameters*

There were slight differences in the beam parameters in the standard libraries used for the irradiation of the PMMA setup. The small mismatch between the beam energies of helium and carbon in the measurements with the PMMA phantoms leads to a sub-millimetre shift of the helium and carbon curves relative to each other compared to an actual mixed beam. This small shift has no qualitative effect on the reported results since the slope of the carbon curve beyond the Bragg peak is small and does not exhibit any prominent features. In the case of the pelvis phantoms, a smaller helium spot was used compared to the carbon spot, resulting in less range mixing (caused by lateral tissue inhomogeneities) as would have been observed for a real mixed beam.

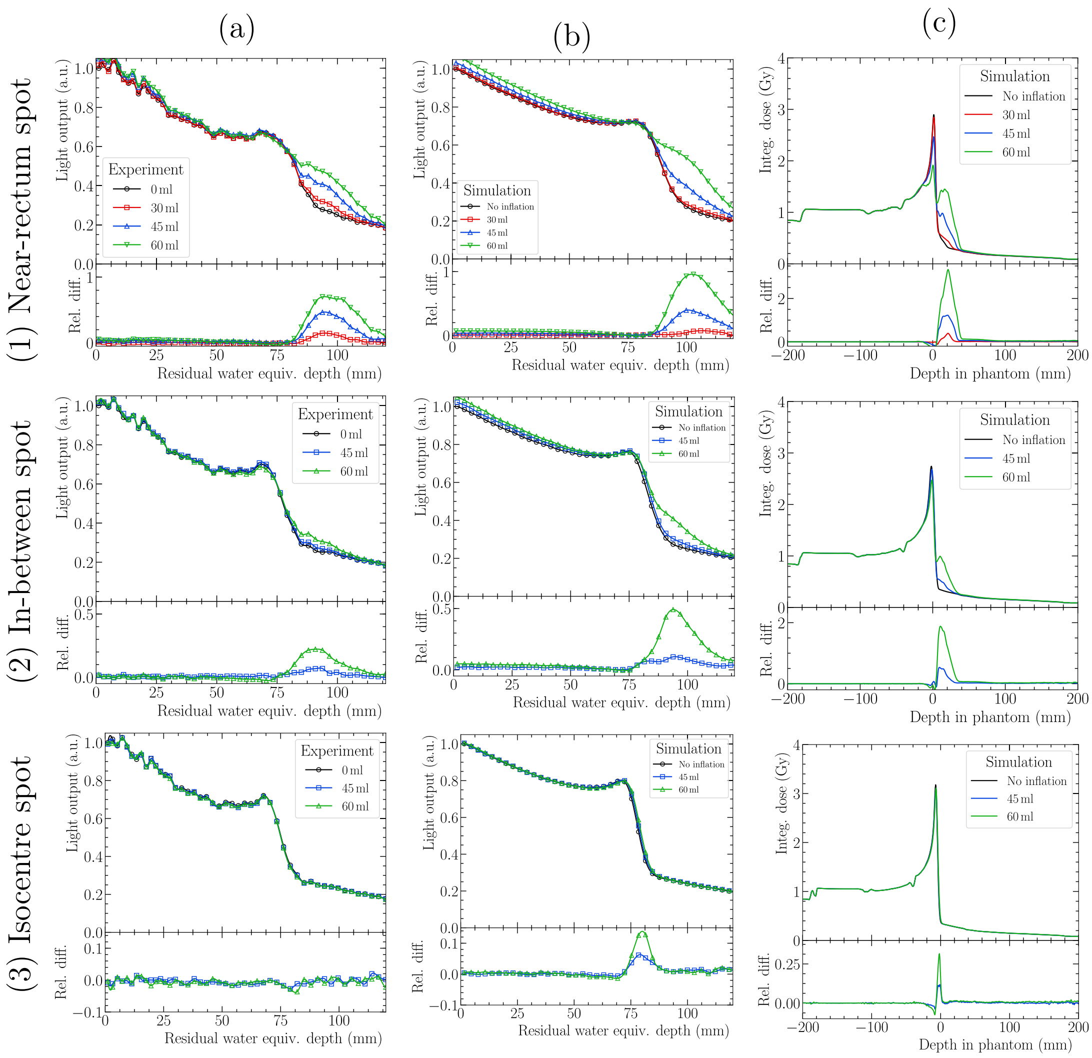

Figure 6. Detector response to different inflation stages of a rectal balloon placed in the rectum near the prostate for different beam spot positions: measured (left column) and simulated (middle column) helium/carbon beam signal in the detector. For comparison, the integrated dose to the phantom as a function of distance to the isocentre (right column) is shown. The dose considers both the helium and carbon beams. (a) Experiment. (b) Simulation. (c) Patient dose (sim.).

4.1.4. *Positioning uncertainty*

Since the HIT experiment cave does not feature an in-room imaging system, a source of uncertainty was the correct positioning of the phantoms relative to the beam, compared with the treatment planning and the simulation. For the PMMA setup, the slit was centered on the beam axis marked by the in-room laser positioning system by opening the two PMMA slabs symmetrically. In general a good agreement of simulation and measurement was observed here, suggesting an accurate phantom positioning for the measurement. For the ADAM phantom, the location of the target isocentre was marked on the phantom surface based on the treatment plan CT scan. This process already introduced some positioning uncertainty due to inaccuracies in the marking by hand. For the ADAM-PETer phantom, the target isocentre was already marked on the outside of the phantom with CT bead markers from an earlier experiment which can be seen as bright spots on the phantom contour in figure 2(b). The in-room positioning was then performed using the available laser positioning system. Nevertheless, for both pelvis phantoms, all investigated beam spots were more than 2 mm away from the treatment field edge. Therefore, it can be argued that despite positioning uncertainties, the results obtained still depict a realistic scenario.

In the ADAM-PETer measurements, an additional source of uncertainty was the manual rotation of the phantom, since no automatic rotation was available. Here, the angle relative to the isocentre position was manually drawn on the phantom and is therefore subject to the same uncertainties mentioned above. Nevertheless, the measurements serve to qualitatively demonstrate the feasibility of observing small patient rotations/movements with a mixed helium/carbon beam. It is important to mention that the CT bead markers were left on the ADAM-PETer phantom during irradiation as well as in the simulation. While being made from metal, they where spherical with a diameter of only 1.27 mm and are not expected to have affected the measurement.

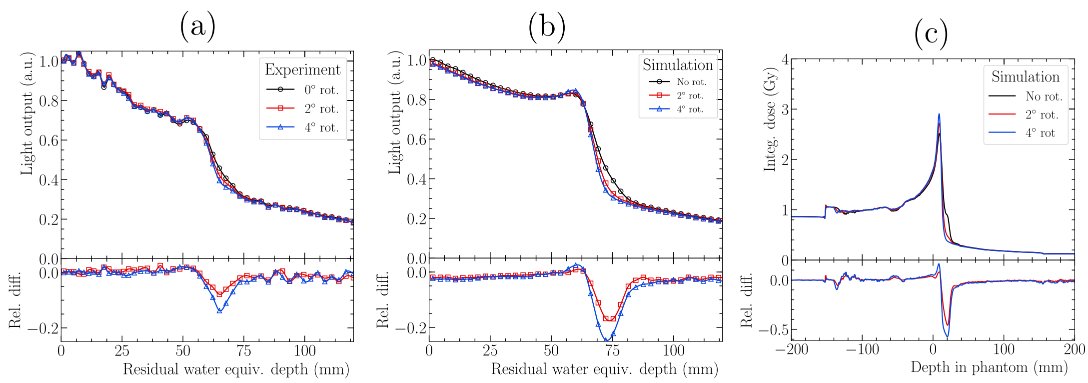

Figure 7. Result for different beam angles entering the phantom: measured (a) and simulated (b) helium/carbon signal in the detector. (c) Shows the integrated dose to the patient as function of the distance to the isocentre. The dose considers both the helium and the carbon ion.

4.1.5. Monte-Carlo simulation

The major uncertainty in the Monte-Carlo simulation was the modeling of the phantom materials. Especially, for the anthropomorphic phantoms, this introduced differences between the measured and the simulated helium range. Due to noise and beam hardening artefacts in the CT image as well as tissue substitute materials with overlapping Hounsfield unit range (Niebuhr *et al* 2019), it was not possible to match the simulated and real composition perfectly with the method used in this work. For example, for the ADAM phantoms, the silicone organ shells were simulated as inner bone, due to the overlap in Hounsfield unit ranges for the two materials. Still, the observed signal variations introduced by the investigated changes in the treated geometry qualitatively agree well between simulation and experiment. However, when using Monte-Carlo as a basis for comparison to generate online treatment feedback (see discussion below), using more sophisticated methods to generate the Monte-Carlo material composition—e.g. using a dual-energy CT image as the basis (Hünemohr *et al* 2014, Lalonde and Bouchard 2016)—would be adequate. Implementing such methods, however, was beyond the scope of this work.

4.2. Using a mixed helium/carbon beam for treatment monitoring

This work highlights the potential of mixing a small amount of helium ions with a therapeutic carbon–ion beam for observing changes in the treated anatomy. This corroborates previous studies using treatment planning software (Graeff *et al* 2018) and experimental investigations with protons in place of helium ions (Mazzucconi *et al* 2018). Since the helium energies are fixed by the carbon energies from the treatment plan, the helium/carbon beam mixing technique is limited to treatment directions were the proximal target edge is located deeper than 1/3 of the patient WET in that direction. Otherwise, the helium ions would not have sufficient energy to fully cross the patient leading to the helium Bragg peak being located in healthy tissue. However, this limitation can potentially be overcome by selecting the treatment direction accordingly, if the gained additional information from the helium ions out-weights the drawback of a non-ideal beam direction. A thorough evaluation of patient data is needed to assess the applicability of the helium/carbon mixing method for different treatment sites.

A general drawback of the method is that the helium ions are not only sensitive to range changes that affect the carbon ions, but also to every change that occurs distal to the tumour. However, integrating the tissue properties over the whole thickness of the patient rather than just up to the tumour volume is true for any radiography-based system. For patient sites where there is known anatomical motion distal to the tumour, such as lung cases, a pre-treatment 4D-CT should be used to relate a given motion phase to the helium range including also the distal anatomy. For prostate cases, on the other hand, this is a less critical limitation. Here, the expected motion scenarios involve, for example, hip motion/rotation, bladder and rectum filling, as well as muscle contractions around the prostate (Langen *et al* 2008), which should have an effect on both the helium and carbon range. Additionally, since the prostate lies centrally in the patient for lateral beam directions, all treatment plan energies should be sufficiently high for the helium ions to fully cross the patient. Moreover, prostate cases might benefit greatly from the helium/carbon mixing method: the irregularity and randomness of the motion patterns makes prostate motion hard to predict or mitigate in scanned ion-beam therapy (Ammazzalorso *et al* 2014), which is why online treatment feedback would be highly advantageous. This is even more important when considering hypo-fractionated carbon-beam therapy.

The biggest advantage of the helium/carbon mixing method is the high sensitivity. With the system used in this work, range changes as small as 1 mm of less than a quarter particles in a pencil beam were observable. Furthermore, this sensitivity is achieved for a small number of incident particles per spot since only very few helium ions are required for a range measurement. It is important to note that for the measurements shown in this work a relatively large number of particles was integrated (21 readout frames summing up to $\sim 6.7 \times 10^7$ integrated particles for the PMMA phantom measurements) compared to the number of particles encountered in clinical pencil beams. This is due to the detector prototype used not being the ideal detection system for the helium/carbon beam mixing method, since it was developed as a quality assurance device for proton beams. The amount of necessary particles could, however, be reduced by using a more sensitive photodetector. A fast-enough detector might even enable the acquisition of multiple range samples (snap shots) per beam spot (provided that the spot contains enough particles) in order to observe motion trends.

This work indicates that the previously suggested 10:1 ratio between primary carbon ions and helium ions is indeed useful for detecting changes in the treated anatomy. However, the optimal mixing ratio will depend on the detector used as well as on the technical aspects of the acceleration of the beam in the synchrotron. Furthermore, the sensitivity of the method also depends on the beam spot size, since with a smaller beam spot size small inhomogeneities would affect a larger portion of the pencil beam particles. However, for the range telescope used in this work, the lateral position of the artefact causing the observed range differences could not be determined with better precision than the pencil beam size without further processing. In order to achieve a better spatial resolution, the information of adjacent spots in the treatment plan could be matched (Hammi *et al* 2017) or position sensitive detectors could be included to the setup (see for example (Krah *et al* 2018) for an overview over the spatial resolution of different particle imaging setups).

It is not trivial to quantify the observed changes in the helium range due to the strong range mixing in heterogeneous materials. A possible option would be to conduct a multi Bragg-peak fit similar to the methodology developed in Krah *et al* (2015). In the work described here, the relative difference to a reference measurement was used to quantify range changes. This enables quantifying small changes compared to the expected signal without relying on a single point of reference and without the need to perform a fit to the signal. The latter feature could be of importance when using a mixed helium/carbon beam for generating online feedback during the treatment where computational speed is a necessity. On the other hand, using the relative difference compared to the expected signal as a metric requires generating a reference curve for every beam spot. This could potentially be accomplished using Monte Carlo simulations at the treatment planning stage that include an accurate description of the detector output (including spatial variations in the detector response/scintillation light quenching) and patient geometry, as has been suggested in Mazzucconi *et al* (2018). As stated above, this would require sophisticated tissue decomposition methods, as well as accurate physics models in the simulation. Nevertheless, an accurate representation of the patient is crucial for treatment planning and, hence, an observed deviation from the expected signal would point towards a potential uncertainty in the treatment plan.

Finally, a mixed helium/carbon beam would offer the potential for post-treatment reconstruction of 2D images of the treated anatomy for each iso-energy slice using the techniques developed for particle radiographic imaging (see Parodi (2014), Krah *et al* (2015)). This could be useful in post-treatment patient-specific quality assurance and dose accumulation.

However, whilst the presented results are indicative of the potential of a mixed beam, they can only serve as a conceptual assessment of the method since they were produced with sequentially irradiated helium/carbon beams. Definitive statements of the usefulness of such a technique can only be made based on a real mixed beam.

4.3. Acceleration of a mixed helium/carbon beam

As also reported in Mazzucconi *et al* (2018), the most straightforward way to generate a mixed beam would be to mix the two ions at the sources. However, at HIT, a reasonable current of $^{12}C^{6+}$ cannot be extracted from the sources. Hence, one would extract $^{12}C^{3+}$ and $^{4}He^{+}$ from a source running with methane[10] as the main gas and helium as the support gas. With a similar mass/charge ratio (A/q $\approx$ 4), the partially stripped ions could pass the injection beam line together. However, the HIT LINAC pre-accelerator is optimised to accelerate ions with A/q $\leqslant$ 3 and cannot accelerate ions with A/q $=$4. Therefore, a real mixed helium/carbon beam could not yet be delivered. A potential workaround to this issue could be to fully strip the ions before the LINAC instead of the current stripping after the LINAC, although this is usually avoided since the stripping efficiency decreases with decreasing beam energy (Bryant *et al* 2000). Another possibility would be to achieve the beam mixing in the synchrotron by sequentially injecting the different ions. Since $^{16}O^{4+}$ could also pass the low energy beam transport together with $^{12}C^{3+}$ and $^{4}He^{+}$, mixing the beam inside the synchrotron might be preferable in order to avoid beam contamination with oxygen ions. The acceleration of a mixed beam will be the subject of further investigation. Nevertheless, since a great effort is usually made to avoid the contamination of the accelerated ion beams with ions of similar mass/charge ratio (see Winkelmann *et al* (2008)), there is a strong reasoning that such a contamination could also be generated deliberately. If a mixed beam in the synchrotron can be generated, stable extraction, beam focusing and pencil beam scanning will add further complexity. Still, from the results presented

[10] For the usually used CO_2 gas, the $^{12}C^{3+}$ peak in the source spectrum would overlap with the $^{16}O^{4+}$ peak.

in this work it is possible to conclude that the concept of a mixed beam for simultaneous treatment and imaging deserves further investigation.

4.4. Advantages of beam mixing versus sequential irradiation

Given the complexity of the acceleration of a mixed beam, the question arises if intra-fractional treatment monitoring could also be achievable with sequentially irradiated beams. Sequential beams come at the advantage of being easier to generate compared to a mixed beam. Moreover, the verification beam would not be limited by the parameters of the treatment plan. For patient sites subject to slow motion, sequential verification and treatment beams could provide useful information, if fast switching of ion sources or beam energy is technically feasible which is currently being investigated at HIT (Schömers *et al* 2017). In that case, changes would be detected with a probably tolerable delay, depending on the rate of verification to treatment spills and the time needed for switching sources/beam energy. Still, an online range estimate provided by a mixed beam would improve the potential for reduction of unwanted dose delivery and the accuracy of post hoc dose reconstruction for adaptive therapy.

For the treatment of moving targets, especially those with strong range changes such as lung tumors, a mixed beam would be most advantageous. Here, online motion information is most relevant, even if it is only used for dose reconstruction and possible adaptation of following fractions. An important aspect is also that with a mixed beam every spot in a treatment plan could be monitored without prolonging the treatment duration. This would be preferential for the clinical environment at an ion-beam therapy facility where short treatment duration is highly desired (Schömers *et al* 2017). Nevertheless, in future studies, the usefulness of sequential beams for verification should also be further evaluated especially for static or non-periodically moving targets such as the prostate.

5. Conclusion

In this work the use of a mixed helium/carbon beam for monitoring intra-fractional anatomical changes was investigated using a novel range telescope. It was demonstrated that with a mixed beam, range changes as small as 1 mm of only a fraction of the beam width could be observed with the system despite the presence of range mixing. Using two anthropomorphic phantoms, the method's use in more realistic clinical cases was investigated. Here, it was demonstrated that a mixed helium/carbon beam could be useful for observing bowel gas movements and small patient rotations. A limitation of the technique is that the helium energies are determined by the carbon treatment plan and thus might not have sufficient energy to cross the patient for all treatment fields/patient sites. Furthermore, the helium signal will integrate any uncertainty located distal to the carbon peak. Future studies should hence involve 4D patient data to identify patient sites that would benefit most from the technique. The generation of a real mixed helium/carbon beam at a synchrotron accelerator is a subject for further investigations.

Acknowledgments

The authors would like to thank the Heidelberg Ion-Beam Therapy Centre (HIT) for providing the beam time and their excellent help in setting up the experiments. We thank Tim Winkelmann (HIT) for insightful discussions and exchanges regarding the HIT sources. Maria Martisikova (DKFZ) is acknowledged for initiating the implementation of the high helium beam energies. The authors thank Amit B A Bennan (DKFZ) for helping with the MatRad treatment planning software. The DKFZ phantom workshop is gratefully acknowledged for providing the phantoms used in this study. LV is funded by a scholarship of the Helmholtz International Graduate School (HIGS, Heidelberg, Germany). LK has received funding from the European Union's Horizon 2020 research and innovation programme under the Marie Sklodowska–Curie Grant agreement No. 675265, OMA—Optimization of Medical Accelerators.

Author contributions

LV was in charge of planning and preparing the experiments and carried out the simulations presented in this work. LK operated the detector during the experiment and conducted the processing of the experimental data. LV and LK equally shared the writing of the manuscript and the analysis/discussion of the acquired results. All authors contributed significantly to the presented work.

ORCID iDs

L Volz https://orcid.org/0000-0003-0441-4350
C Graeff https://orcid.org/0000-0002-5296-7649
R Radogna https://orcid.org/0000-0002-1094-5038
S Jolly https://orcid.org/0000-0002-2713-0732

References

Agostinelli S *et al* 2003 GEANT4—a simulation toolkit *Nucl. Instrum. Methods Phys. Res.* A **506** 250–303

Allison J *et al* 2006 Geant4 developments and applications *IEEE Trans. Nucl. Sci.* **53** 270–8

Allison J *et al* 2016 Recent developments in GEANT4 *Nucl. Instrum. Methods Phys. Res.* A **835** 186–225

Ammazzalorso F, Graef S, Weber U, Wittig A, Engenhart-Cabillic R and Jelen U 2014 Dosimetric consequences of intrafraction prostate motion in scanned ion beam radiotherapy *Radiother. Oncol.* **112** 100–5

Arico G 2016 Ion spectroscopy for improvement of the physical beam model for therapy planning in ion beam therapy *PhD Thesis* The Faculty of Physics and Astronomy, Heidelberg University

Berger M J, Coursey J S, Zucker M A and Chang J 2005 *ESTAR, PSTAR and ASTAR: Computer Programs for Calculating Stopping–Power and Range Tables for Electrons, Protons and Helium Ions* (National Institue of Standards and Technology) (http://physics.nist.gov/Star)

Bert C, Grözinger S O and Rietzel E 2008 Quantification of interplay effects of scanned particle beams and moving targets *Phys. Med. Biol.* **53** 2253–65

Böhlen T T, Cerutti F, Dosanjh M, Ferrari A, Gudowska I, Mairani A and Quesada J M 2010 Benchmarking nuclear models of FLUKA and GEANT4 for carbon ion therapy *Phys. Med. Biol.* **55** 5833–47

Birks J B 1951 Scintillations from organic crystals: specific fluorescence and relative response to different radiations *Proc. Phys. Soc.* A **64** 874–7

Bryant P J *et al* 2000 *Proton-Ion Medical Machine Study (PIMMS)* (Myrin: CERN) p 2

Collins-Fekete C A, Brousmiche S, Hansen D C, Beaulieu L and Seco J 2017 Pre-treatment patient-specific stopping power by combining list-mode proton radiography and x-ray CT *Phys. Med. Biol.* **62** 6836

Dolde K, Naumann P, Dávid C, Gnirs R, Kachelrieß M, Lomax A J, Saito N, Weber D C, Pfaffenberger A and Zhang Y 2018 4D Dose calculation for pencil beam scanning proton therapy of pancreatic cancer using repeated 4DMRI datasets *Phys. Med. Biol.* **63** 165005

Dudouet J, Cussol D, Durand D and Labalme M 2014 Benchmarking GEANT4 nuclear models for hadron therapy with 95 MeV/nucleon carbon ions *Phys. Rev.* C **89** 054616

Ferrero V *et al* 2018 Online proton therapy monitoring: clinical test of a silicon-photodetector-based in-beam PET *Sci. Rep.* **8** 4100

Graeff C, Weber U, Schuy C, Saito N, Volz L, Piersimoni P, Seco J and Kraemer M 2018 [oa027] Helium as a range probe in carbon ion therapy *Phys. Med.* **52** 11

Haberer T, Debus J, Eickhoff H, Jäkel O, Schulz-Ertner D and Weber U 2004 The Heidelberg Ion Therapy Center *Radiother. Oncol.* **73** S186–90

Hammi A, Lomax T and Weber D 2017 Su-f-601-1: a new technique for increasing spatial resolution of proton radiography *Presented at the American Association of Physics in Medicine Annual Meeting (Denver, USA)* (www.aapm.org/meetings/2017AM/PRAbs.asp?mid=127 aid=37891)

Homolka N *et al* 2019 Pv-0479: development of an anthropomorphic multimodality pelvis phantom for PET/MRI-and CT-based radiation treatment planning of prostate cancer *Radiother. Oncol.* **133**

Horst F *et al* 2019 Measurement of ^{4}He charge- and mass-changing cross sections on H, C, O, and Si targets in the energy range 70–220 MeV/u for radiation transport calculations in ion-beam therapy *Phys. Rev.* C **99** 014603

Hueso-González F, Rabe M, Ruggieri T A, Bortfeld T and Verburg J M 2018 A full-scale clinical prototype for proton range verification using prompt gamma-ray spectroscopy *Phys. Med. Biol.* **63** 185019

Hünemohr N, Paganetti H, Greilich S, Jäkel O and Seco J 2014 Tissue decomposition from dual energy CT data for MC based dose calculation in particle therapy *Med. Phys.* **41** 061714

Kanai T, Furusawa Y, Fukutsu K, Itsukaichi H, Eguchi-Kasai K and Ohara H 1997 Irradiation of mixed beam and design of spread-out bragg peak for heavy-ion radiotherapy *Radiat. Res.* **147** 78–85

Kleffner C, Ondreka D and Weinrich U 2009 The Heidelberg Ion Therapy (HIT) accelerator coming into operation *AIP Conf. Proc.* **1099** 426–8

Krah N, Khellaf F, Létang J M, Rit S and Rinaldi I 2018 A comprehensive theoretical comparison of proton imaging set-ups in terms of spatial resolution *Phys. Med. Biol.* **63** 135013

Krah N, Testa M, Brons S, Jäkel O, Parodi K, Voss B and Rinaldi I 2015 An advanced image processing method to improve the spatial resolution of ion radiographies *Phys. Med. Biol.* **60** 8525

Lalonde A and Bouchard H 2016 A general method to derive tissue parameters for Monte-Carlo Dose calculation with multi-energy CT *Phys. Med. Biol.* **61** 8044

Langen K M, Willoughby T R, Meeks S L, Santhanam A, Cunningham A, Levine L and Kupelian P A 2008 Observations on real-time prostate gland motion using electromagnetic tracking *Int. J. Radiat. Oncol. Biol. Phys.* **71** 1084–90

Mazzucconi D, Agosteo S, Ferrarini M, Fontana L, Lante V, Pullia M and Savazzi S 2018 Mixed particle beam for simultaneous treatment and online range verification in carbon ion therapy: proof-of-concept study *Med. Phys.* **45** 5234–43

Niebuhr N I, Johnen W, Echner G, Runz A, Bach M, Stoll M, Giske K, Greilich S and Pfaffenberger A 2019 The ADAM-pelvis phantom—an anthropomorphic, deformable and multimodal phantom for MRgRT *Phys. Med. Biol.* **64** 04NT05

Niebuhr N I, Johnen W, Güldaglar T, Runz A, Echner G, Mann P, Möhler C, Pfaffenberger A, Jäkel O and Greilich S 2016 Technical note: radiological properties of tissue surrogates used in a multimodality deformable pelvic phantom for MR-guided radiotherapy *Med. Phys.* **43** 908–16

Paganetti H 2012 Range uncertainties in proton therapy and the role of Monte-Carlo simulations *Phys. Med. Biol.* **57** R99

Parodi K 2014 Heavy ion radiography and tomography *Phys. Med.* **30** 539–43 (Particle Radiosurgery Conference)

Parodi K and Polf J C 2018 *In vivo* range verification in particle therapy *Med. Phys.* **45** e1036–50

Schömers C, Feldmeier E, Galonska M, Horn J, Peters A and Haberer T 2017 Thpva083: first tests of a re-accelerated beam at Heidelberg Ion-Beam Therapy Center (HIT) *Proc. of IPAC2017* ed V R W Schaa *et al* (JACoW) (https://doi.org/10.18429/JACoW-IPAC2017-THPVA083)

Seco J, Robertson D, Trofimov A and Paganetti H 2009 Breathing interplay effects during proton beam scanning: simulation and statistical analysis *Phys. Med. Biol.* **54** N283–94

Tripathi R, Cucinotta F and Wilson J 1999 Accurate universal parameterization of absorption cross sections III—light systems *Nucl. Instrum. Methods Phys. Res.* B **155** 349–56

Wieser H P *et al* 2017 Development of the open-source dose calculation and optimization toolkit matRad *Med. Phys.* **44** 2556–68

Winkelmann T, Cee R, Haberer T, Naas B, Peters A, Scheloske S, Spädtke P and Tinschert K 2008 Electron cyclotron resonance ion source experience at the heidelberg ion beam therapy center *Rev. Sci. Instrum.* **79** 02A331